Weak Ferromagnetism in Altermagnets from Alternating g-Tensor Anisotropy

Daegeun Jo,[1,2,*] Dongwook Go,[3,4] Yuriy Mokrousov,[3,4] Peter M. Oppeneer,[1,2]
Sang-Wook Cheong,[5,†] and Hyun-Woo Lee[6,‡]
[1]*Department of Physics and Astronomy, Uppsala University, P.O. Box 516, SE-75120 Uppsala, Sweden*
[2]*Wallenberg Initiative Materials Science for Sustainability, Uppsala University, SE-75120 Uppsala, Sweden*
[3]*Institute of Physics, Johannes Gutenberg University Mainz, 55099 Mainz, Germany*
[4]*Peter Grünberg Institut, Forschungszentrum Jülich and JARA, 52425 Jülich, Germany*
[5]*Rutgers Center for Emergent Materials and Department of Physics and Astronomy, Rutgers University,*
Piscataway, New Jersey 08854, USA
[6]*Department of Physics, Pohang University of Science and Technology, Pohang 37673, Korea*

(Received 23 August 2024; accepted 21 April 2025; published 16 May 2025)

Altermagnets are magnetic materials with antiferromagnetic spin ordering but exhibit ferromagnetic properties. Understanding the microscopic origin of the latter is a central problem. Ferromagnetlike properties such as the anomalous Hall effect are linked with weak ferromagnetism, whose microscopic origin in altermagnets remains unclear however. We show theoretically that the alternating g-tensor anisotropy in altermagnets can induce weak orbital ferromagnetism even when the Dzyaloshinskii-Moriya interaction is forbidden. We demonstrate this mechanism to explain weak ferromagnetism for both collinear and noncollinear spin altermagnets. Our findings provide new insights into the origin of weak ferromagnetism and suggest orbital-based ways for manipulating magnetic configurations in altermagnets.

DOI: 10.1103/PhysRevLett.134.196703

Magnetic materials have traditionally been categorized by spin ordering: ferromagnets (FMs) with parallel spins and antiferromagnets (AFMs) with antiparallel spins. However, recent studies [1–20] have highlighted the significant role of the interplay between spin ordering and local crystal structure surrounding magnetic atoms in characterizing magnetic materials. This insight has led to the classification of a new type of magnetism, dubbed altermagnetism [19–23]. Altermagnets (AMs) have antiferromagnetic spin ordering with alternating local crystal structures at the sublattices. In view of the symmetry analysis based on the spin group theory, the alternating local crystal structure is crucial for the FM-like properties of the AMs. First, the electronic bands are spin-split [24–26]. In the presence of spin-orbit coupling (SOC), they can exhibit further FM-like behavior such as the magneto-optical effect [14,27] and the anomalous Hall effect [5,28,29]. Therefore, AMs offer potential for novel spintronic applications [30–32], combining the benefits of both FMs [33,34] and AFMs [35,36].

Despite FM-like behavior being compatible with symmetry, a fundamental question still remains unanswered: What is a *microscopic* defining feature of AMs that distinguishes them from conventional AFMs and gives rise to their FM-like behavior? Recently, ferroic ordering of magnetic octupoles has been proposed as a microscopic order parameter to describe d-wave AMs [37]. According to a Landau theory augmented by spin-space symmetries, this magnetic octupole can couple linearly to the magnetic dipole through SOC [38], enabling weak ferromagnetism (WFM) in AMs [38–45] and their FM-like behavior. However, the microscopic origin of WFM in AMs remains unclear. Although the Dzyaloshinskii-Moriya interaction (DMI) [46,47] can induce the WFM in some AMs such as α-Fe_2O_3 [47] and La_2CuO_4 [48], it cannot explain the substantial orbital magnetization of rutile-type [5,14] and Mn_3Sn-type [49–51] AMs predicted by first-principles calculations, necessitating deeper investigation into the origin of the WFM in AMs.

In this Letter, we study a thus far unexplored origin of WFM in AMs: alternating g-tensor anisotropy. The g-tensor not only characterizes the spin exchange energy but also reflects the structural anisotropy, prompting us to examine its role in AMs. We demonstrate theoretically that the alternation of the g-tensor anisotropy among sublattices of AMs can naturally lead to WFM, primarily driven by the orbital moment, even when the DMI is forbidden. A wide range of AMs exhibit WFM either intrinsically (type-I AMs) or under strain (type-II AMs) [43]. This mechanism

---

[*] Contact author: daegeun.jo@physics.uu.se

[†] Contact author: sangc@physics.rutgers.edu

[‡] Contact author: hwl@postech.ac.kr

extends beyond conventional AMs with collinear spin ordering and straightforwardly applies to AMs with noncollinear spin ordering [43]. Our findings not only provide insights into FM-like properties of AMs but also offer a fresh perspective on previous studies of WFM in various compounds [46–48,50–55].

The spectroscopic g-tensor [56] is defined as the ratio of the total magnetic moment to the spin angular momentum, which can be represented by a 3×3 matrix $\mathbf{g}$. In many high-symmetry systems, principal axes can be chosen such that the orbital and spin angular momenta are aligned with them. In this case, $\mathbf{g}$ can be expressed as a diagonal matrix with elements

$$g_\alpha = 2 + \frac{\langle L_\alpha \rangle}{\langle S_\alpha \rangle}, \qquad (1)$$

where $\langle L_\alpha \rangle$ and $\langle S_\alpha \rangle$ are expectation values of orbital and spin angular momentum operators $\mathbf{L}$ and $\mathbf{S}$ along the principal axis α, respectively. For example, let us consider a FM exhibiting the spin S_0 along the α axis in the absence of SOC, where the orbital is quenched. When weak SOC is taken into account, a finite $\langle L_\alpha \rangle$ is induced, which is linear in the SOC strength λ_{SO} [57]. On the other hand, the spin-orbit correction to the spin is at least second order [51], i.e., $\langle S_\alpha \rangle = S_0 + O(\lambda_{\mathrm{SO}}^2)$. Therefore, in the weak SOC regime, the SOC-induced magnetic moment originates primarily from the orbital moment, causing g_α to deviate from 2 by an amount proportional to the induced orbital moment or λ_{SO} [52].

The anisotropic orbital moment is an essential ingredient of our discussion. If the crystal structure is anisotropic, the SOC-induced orbital moment depends on the spin exchange field direction $\hat{\mathbf{s}}$ due to the interplay between spin and crystal structure, which is also known to be responsible for magnetic anisotropy energy [57]. Here, we focus on its influence on the g-tensor. Consider a magnetic atom subject to an electrical potential featuring uniaxial anisotropy with principal axes $\hat{\mathbf{e}}_\parallel$ and $\hat{\mathbf{e}}_\perp$ [Fig. 1(a)]. We compare two configurations where orbital and spin angular momenta, aligning with $\hat{\mathbf{s}}$, are oriented either along $\hat{\mathbf{e}}_\parallel$ or $\hat{\mathbf{e}}_\perp$. Based on the previous discussion, we expect that the orbital angular momenta $L_\parallel \neq L_\perp$ are linearly proportional to the SOC strength, while the spin angular momenta $S_\parallel$ and $S_\perp$ remain approximately equal to S_0. Consequently, the g-tensor can be expressed as $\mathbf{g} = \mathrm{diag}(g_\perp, g_\perp, g_\parallel)$, where $g_{\parallel(\perp)} \approx 2 + L_{\parallel(\perp)}/S_0$. This leads us to define the g-tensor anisotropy Δg as

$$\Delta g \equiv g_\parallel - g_\perp \approx \frac{L_\parallel - L_\perp}{S_0}, \qquad (2)$$

which can be experimentally evaluated from the ferromagnetic resonance spectroscopy [58]. Although we have assumed a ferromagnetic atom, our discussion can be generalized to altermagnetic systems by defining the g-tensor locally for each magnetic atom.

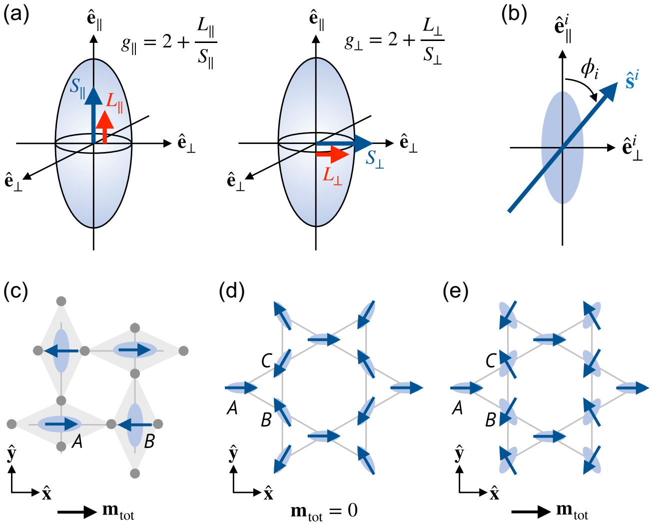

FIG. 1. (a) Schematic illustration of the g-tensor anisotropy for a magnetic atom. The blue ellipsoids illustrate uniaxial anisotropy with principal axes $\hat{\mathbf{e}}_\parallel$ and $\hat{\mathbf{e}}_\perp$. $S_{\parallel(\perp)}$ and $L_{\parallel(\perp)}$ are the spin and orbital angular momenta along $\hat{\mathbf{e}}_{\parallel(\perp)}$, respectively. (b) Example of the local structure of the magnetic sublattice i in an AM. (c)–(e) Altermagnetic systems with alternating g-tensor anisotropy. Panels (c) and (e) exhibit the WFM (type-I AM), while panel (d) does not (type-II AM).

Now, we show that Δg combines with the alternating local crystal structure to generate the WFM of AMs. We consider a prototypical altermagnetic system. The ith magnetic atom is surrounded by a crystalline potential with uniaxial anisotropy, having principal axes $\hat{\mathbf{e}}^i_\parallel$ and $\hat{\mathbf{e}}^i_\perp$ [Fig. 1(b)]. The local spin $\langle \mathbf{S}^i \rangle = S_0 \hat{\mathbf{s}}^i$ makes an angle ϕ_i with $\hat{\mathbf{e}}^i_\parallel$, satisfying $\sum_i^N \hat{\mathbf{s}}^i = 0$, where N is the number of atoms in a unit cell. The local g-tensor $\mathbf{g}^i = \mathrm{diag}(g_\perp, g_\perp, g_\parallel)$ is defined in terms of the principal axes at each site. $g_\parallel$ and $g_\perp$ are independent of the sublattice, provided that the local crystal structures at each site are connected by rotational symmetry to each other [e.g., Figs. 1(c)–1(e)]. Thus, the total magnetic moment $\mathbf{m}_{\mathrm{tot}} = -(\mu_{\mathrm{B}}/\hbar) \sum_i^N \mathbf{g}^i \cdot \langle \mathbf{S}^i \rangle$ is proportional to $\sum_i^N [g_\parallel \cos\phi_i \hat{\mathbf{e}}^i_\parallel + g_\perp (\hat{\mathbf{s}}^i - \cos\phi_i \hat{\mathbf{e}}^i_\parallel)]$ and given by

$$\mathbf{m}_{\mathrm{tot}} = -\frac{\mu_{\mathrm{B}}}{\hbar} \Delta g S_0 \mathbf{s}_\parallel, \qquad \mathbf{s}_\parallel = \sum_i^N \cos\phi_i \hat{\mathbf{e}}^i_\parallel, \qquad (3)$$

to first order in SOC. Equation (3) is the main result of our paper; it clearly demonstrates that the net magnetic moment of AMs is proportional to Δg instead of the electron spin g-factor 2 for strong FMs. Our theory generalizes the single-ion anisotropy picture [52] by incorporating the orbital moment, providing a new perspective on WFM.

Since $\mathbf{m}_{\rm tot}$ is dominated by the orbital contribution, it is naturally related to orbital-dominated anomalous Hall AFMs [51,59]. Notably, the direction of $\mathbf{m}_{\rm tot}$ is determined by $\mathbf{s}_{\parallel}$, representing the projection of spins with respect to local crystalline axes. This direction can differ from that of the DMI-induced net moment, and $\mathbf{m}_{\rm tot}$ can be nonzero even when the DMI is forbidden (see End Matter). Our mechanism based on Δg is thus clearly distinct from the DMI-induced WFM. We further emphasize that our mechanism represents an *intrinsic* property of AMs since it arises from the alternating local crystal structure, which is a defining feature of AMs. By contrast, the origin of the DMI is not inherently related to the alternating local structure.

Here, we examine AMs with collinear spins using Eq. (3). Figure 1(c) shows a two-dimensional square lattice consisting of two magnetic atoms A and B with opposite spins. The gray circles at the corners of the diamonds represent the nonmagnetic atoms, which give rise to the anisotropic crystal potential depicted by blue ellipses. Similar types of structures are commonly found in rutile-type AMs, such as $\mathrm{RuO_2}$ [5], $\mathrm{MnF_2}$ [6], and $\mathrm{NiF_2}$ [52]. For an arbitrary in-plane spin configuration with $\phi_A = \phi$ and $\phi_B = \phi + \pi/2$, Eq. (3) leads to

$$\mathbf{m}_{\rm tot} = -\frac{\mu_{\rm B}}{\hbar}\Delta g S_0(\cos\phi\hat{\mathbf{x}} - \sin\phi\hat{\mathbf{y}}). \tag{4}$$

Interestingly, the predicted $\mathbf{m}_{\rm tot}\|\mathbf{s}_{\parallel} = \cos\phi\hat{\mathbf{x}} - \sin\phi\hat{\mathbf{y}}$ can be either parallel or perpendicular to the Néel vector $\hat{\mathbf{n}} = \cos\phi\hat{\mathbf{x}} + \sin\phi\hat{\mathbf{y}}$ depending on ϕ. This angular dependence is consistent with first-principles calculations for $\mathrm{NiF_2}$ (see End Matter) and $\mathrm{RuO_2}$ [5,14], which cannot be attributed to the DMI. Such AMs exhibiting WFM have been categorized as type-I AMs [43]. Conversely, for the out-of-plane spin configuration with $\hat{\mathbf{s}}^i = \pm\hat{\mathbf{z}}$ (e.g., $\mathrm{CoF_2}$ [60]), implying $\phi_A = \phi_B$, Eq. (3) yields $\mathbf{m}_{\rm tot} = 0$ since the relevant g-tensor anisotropy in this configuration is the difference between two $g_{\perp}$'s. Inducing difference between them by strain can induce net magnetization, which amounts to piezomagnetism [60,61]. This type of AMs, with zero net magnetization and piezomagnetism, has been categorized as type-II AMs [43].

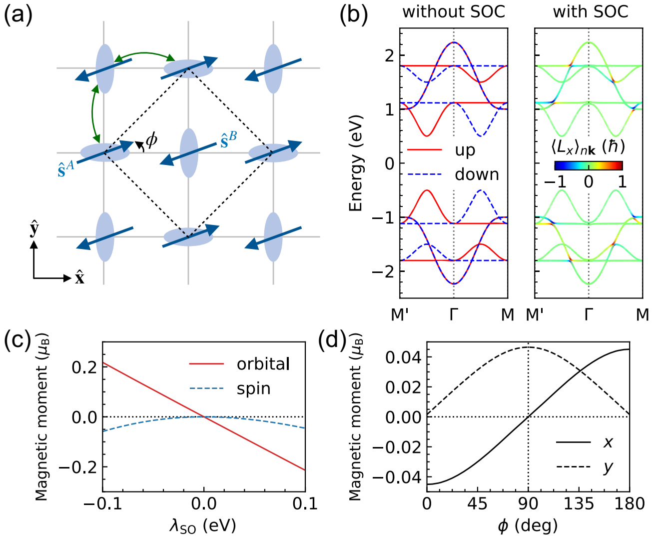

FIG. 2. (a) Schematic illustration of the tight-binding model $\mathcal{H}$ for an AM with collinear spins. The dashed lines represent the unit cell, and the green arrows indicate the nearest-neighbor hoppings. The blue ellipses display the anisotropy. (b) Band structures without (left panel) and with (right panel) SOC. (c) The net orbital and spin magnetic moments at the Fermi energy $E_{\rm F} = -0.9$ eV as a function of the SOC strength $\lambda_{\rm SO}$. (d) x and y components of the total magnetic moment at $E_{\rm F} = -0.9$ eV depending on the spin angle ϕ.

Next, we test the above predictions by performing tight-binding calculations for a two-dimensional square lattice consisting of two magnetic atoms A and B with an antiferromagnetic spin ordering characterized by an angle ϕ [Fig. 2(a)]. Assuming the atomic orbital basis $\{d_{xy}, d_{yz}, d_{zx}\}$ for each atom, the Hamiltonian is written as (see Supplemental Material [62] for details)

$$\mathcal{H} = \sum_{\langle i,j\rangle mn\sigma} t_{ijmn} c^{\dagger}_{im\sigma} c_{jn\sigma} - \frac{J_{\rm sd}}{\hbar}\sum_{in\sigma\sigma'} \hat{\mathbf{s}}^i \cdot c^{\dagger}_{in\sigma}\mathbf{S}_{\sigma\sigma'}c_{in\sigma'} + \frac{\lambda_{\rm SO}}{\hbar^2}\sum_{imn\sigma\sigma'} c^{\dagger}_{im\sigma}\mathbf{L}_{mn}\cdot\mathbf{S}_{\sigma\sigma'}c_{in\sigma'}, \tag{5}$$

where $c^{\dagger}_{in\sigma}$ ($c_{in\sigma}$) is the creation (annihilation) operator of an electron at site i with orbital index n and spin $\sigma = \uparrow, \downarrow$. The first term describes nearest-neighbor hopping, the second term represents the exchange interaction with the molecular field $(J_{\rm sd}/\hbar)\hat{\mathbf{s}}^i$, and the third term corresponds to the atomic SOC, where $\mathbf{L}$ is defined in terms of the atomic orbital basis. Note that this lattice does not contain nonmagnetic atoms in contrast to typical rutile-structure AMs [e.g., Fig. 1(c)]. Thus, Eq. (5) reflects neither local anisotropy nor altermagnetism. To capture the alternating local crystal structure arising from the nonmagnetic atoms, we introduce the sublattice-dependent crystal field to each magnetic atom as follows:

$$\mathcal{H}_{\rm CF} = \frac{\Delta_{\rm CF}}{2}\sum_{i\sigma}\tau\left(c^{\dagger}_{i,yz,\sigma}c_{i,yz,\sigma} - c^{\dagger}_{i,zx,\sigma}c_{i,zx,\sigma}\right), \tag{6}$$

with the sublattice index τ being $+1(-1)$ for $A(B)$. This term leads to the alternating local anisotropy, as depicted by Fig. 2(a), thereby giving rise to altermagnetism.

Figure 2(b) shows the band structures without (left) and with (right) SOC for the total Hamiltonian $\mathcal{H} + \mathcal{H}_{\rm CF}$ with $J_{\rm sd} = 1.0$ eV, $\phi = 0$, $\lambda_{\rm SO} = 0.02$ eV, and $\Delta_{\rm CF} = 1.0$ eV. The nonrelativistic spin splitting alternates in sign between the $\mathbf{k}$ paths from Γ to $\mathrm{M} = (0.5, 0.5)$ and from Γ to $\mathrm{M}' = (-0.5, 0.5)$. With SOC, doubly degenerate d_{xy} bands hybridize with d_{zx} bands, inducing an orbital angular momentum $\langle L_x\rangle_{n\mathbf{k}}$ for each $\mathbf{k}$ point with band n.

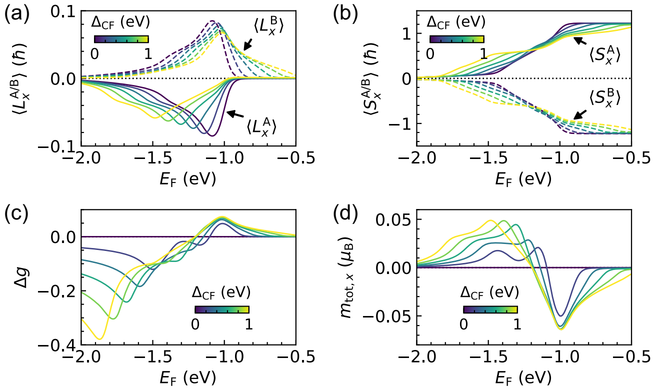

FIG. 3. (a),(b) Fermi energy (E_F) dependences of (a) orbital and (b) spin angular momenta for atom A (solid lines) and atom B (dashed lines) with varying crystal field parameter Δ_{CF}. (c),(d) E_F dependences of (c) g-tensor anisotropy Δg and (d) total magnetic moment $m_{tot,x}$ with varying Δ_{CF}.

The anisotropy of $\langle L_x\rangle_{n\mathbf{k}}$ in $\mathbf{k}$ space results in the net orbital moment, which is linear in λ_{SO} [Fig. 2(c)] and dominant over the net spin moment that is quadratic in λ_{SO}. These features agree with our expectations. Additionally, the ϕ dependence of $\mathbf{m}_{tot}$ [Fig. 2(d)] is consistent with Eq. (4).

Next, we examine the connection between the g-tensor anisotropy and net magnetic moment. For this, we first calculate the orbital (spin) angular momentum projected onto atoms A and B, denoted by $\langle L_x^A\rangle$ and $\langle L_x^B\rangle$ ($\langle S_x^A\rangle$ and $\langle S_x^B\rangle$), respectively, as a function of the Fermi energy E_F and as a function of the alternating crystal field parameter Δ_{CF} in $\mathcal{H}_{CF}$. Figure 3(a) demonstrates that $\langle L_x^A\rangle + \langle L_x^B\rangle$ is zero for $\Delta_{CF} = 0$ and becomes larger in magnitude as Δ_{CF} increases. In contrast, $\langle S_x^A\rangle + \langle S_x^B\rangle$ remains almost zero regardless of Δ_{CF} [Fig. 3(b)]. Then, the g-tensor anisotropy, evaluated by $\Delta g = \langle L_x^A\rangle/\langle S_x^A\rangle - \langle L_x^B\rangle/\langle S_x^B\rangle$, gradually increases with Δ_{CF} [Fig. 3(c)]. Note that the total magnetic moment [Fig. 3(d)] exhibits a clear correlation with Δg. Moreover, we find that the product $\Delta g(|\langle S_x^A\rangle| + |\langle S_x^B\rangle|)/2$ exhibits the essentially identical variation as $m_{tot,x}$ with respect to E_F or Δ_{CF} change, providing further support to Eq. (3).

It is worthwhile to compare the magnitude of the WFM arising from two mechanisms: Δg and the DMI. Spin moments canted by an angle ψ due to the DMI produce a net transverse spin moment of $m_{DMI} = -(\mu_B/\hbar)S_0 \sin\psi$. Given the similarity between this relation and Eq. (4), the comparison between the two effects reduces to that between $\sin\psi$ and Δg. In prototypical DMI antiferromagnets [72], ψ typically reaches the order of 1°, leading to $\sin\psi \approx 0.02$. On the other hand, Δg can reach the order of 0.1, corresponding to an angle of $\sin^{-1}(\Delta g) = 5.7°$, in our model or rutile AMs (see End Matter) in the metallic phase. This illustrates that the WFM arising from Δg can be much larger than that induced by the DMI.

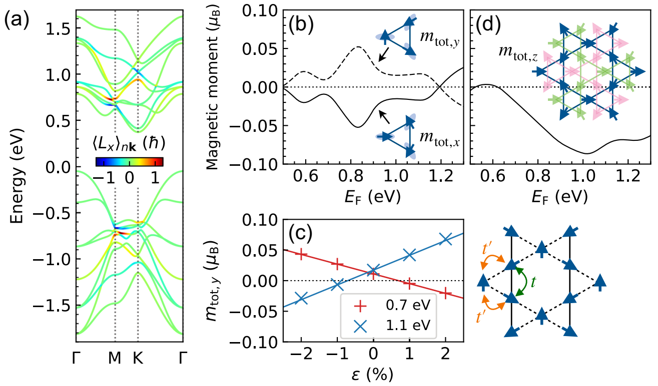

FIG. 4. (a) Band structure of the kagome lattice having an inverse triangular spin structure with $\phi = 0$. (b) Fermi energy (E_F) dependences of the net magnetic moment $m_{tot,x}$ for $\phi = 0$ (solid line) and $m_{tot,y}$ for $\phi = \pi/2$ (dashed line). The insets display the spin configuration for the three sublattices. (c) $m_{tot,y}$ of the distorted kagome lattice (right panel) at $E_F = 0.7$ eV (red + symbols) and $E_F = 1.1$ eV (blue × symbols) with varying strain parameter ε. Solid lines indicate a linear relation between ε and $m_{tot,y}$. (d) E_F dependence of $m_{tot,z}$ for the bulk system with ABC-stacked kagome planes. The inset shows the top view of the structure, where blue, pink, and green layers are stacked in order.

Next, we extend our theory to AMs with noncollinear spin structures [43]. For example, Fig. 1(d) displays a kagome lattice with a triangular spin structure where the spins of sublattices A, B, and C are each rotated by 120° relative to one another and the local g-tensor of each sublattice is anisotropic. In this normal triangular spin structure, the angles between spin and g-tensor's principal axis are identical for all sublattices, i.e., $\phi_A = \phi_B = \phi_C$, which makes $\mathbf{m}_{tot}$ in Eq. (3) zero (type-II AM). On the other hand, for an inverse triangular spin structure [Fig. 1(e)], where the spins are rotated by −120°, Eq. (3) predicts a nonvanishing $\mathbf{m}_{tot}$ (type-I AM). For arbitrary angles, $\phi_A = \phi$, $\phi_B = \phi + 2\pi/3$, and $\phi_C = \phi + 4\pi/3$, $\mathbf{m}_{tot}$ follows Eq. (4) [59]. We note that, in both normal [Fig. 1(d)] and inverse [Fig. 1(e)] triangular spin structures, the DMI does not induce any net spin moment [53] since these spin configurations with complete spin compensation minimize the DMI energy.

We also examine these predictions numerically by applying $\mathcal{H}$ to the kagome lattices (see Supplemental Material [62] for details and parameters used). Since the magnetic atoms themselves in the kagome lattices give rise to the alternating local crystal structure, we consider in our calculation only $\mathcal{H}$ and ignore $\mathcal{H}_{CF}$. For each magnetic atom, the orbital basis $\{d_{3z^2-r^2}, d_{yz}, d_{zx}\}$ is taken into account. The angle between the spin at sublattice A and the x axis is given by ϕ. We first consider the inverse triangular spin structure [Fig. 1(e)]. Its band structure for $\phi = 0$ [Fig. 4(a)] shows band-resolved $\langle L_x\rangle_{n\mathbf{k}}$ summed over three sublattices A, B, and C. Analogous to the collinear spin case, the orbital is the main contribution to $\mathbf{m}_{\rm tot}$. In Fig. 4(b), the solid and dashed lines present the x and y components of $\mathbf{m}_{\rm tot}$ for $\phi = 0$ (e.g., $\mathrm{Mn_3Ge}$ and $\mathrm{Mn_3Ga}$) and $\phi = \pi/2$ (e.g., $\mathrm{Mn_3Sn}$), respectively. Note that they follow the predicted relation $m_{{\rm tot},x}(\phi) = -m_{{\rm tot},y}(\phi + \pi/2)$ [Eq. (4)].

Motivated by an experiment [73] on the piezomagnetic properties of the kagome lattice with the inverse triangular spin structure, we examine the strain effect on $\mathbf{m}_{\rm tot}$. The right panel of Fig. 4(c) shows a distorted kagome lattice, with solid and dashed lines indicating different bond lengths r and r', respectively. Suppose $r' = (1 + \varepsilon)r$ due to the strain with the parameter ε. The original hopping parameter t is then modified to t' under strain, which can be approximated as $t' = t/(1 + \varepsilon)^2$ [74]. We incorporate this effect into the tight-binding model while preserving the lattice structure [62]. The left panel in Fig. 4(c) presents $m_{{\rm tot},y}$ at $E_{\rm F} = 0.7$ eV and $E_{\rm F} = 1.1$ eV, demonstrating a piezomagnetic effect [60]: magnetization is induced by strain linearly. As $\mathbf{m}_{\rm tot}$ for $\varepsilon = 0$ is tiny, $\mathbf{m}_{\rm tot}$ can be easily switched by the piezomagnetic effect, in qualitative agreement with the experiment [73].

For the normal triangular spin structure [Fig. 1(d)], our numerical calculation finds $\mathbf{m}_{\rm tot} = 0$, as predicted by Eq. (3). However, WFM can be induced via symmetry-breaking stacking. For instance, the structures of $\mathrm{Mn_3Rh}$, $\mathrm{Mn_3Ir}$, and $\mathrm{Mn_3Pt}$ consist of kagome planes with ABC-type stacking along the (111) direction [75,76], which breaks the C_{2x} symmetry. To examine these systems, we apply $\mathcal{H}$ to the three-dimensional bulk structure composed of ABC-stacked kagome lattices with the normal triangular spin structure [inset of Fig. 4(d)] [62]. In this system, the off-diagonal g-tensor element $g_{zx} = \langle L_z + 2S_z\rangle/\langle S_x\rangle$ becomes nonzero due to the broken C_{2x} symmetry. As a result, out-of-plane magnetization is induced, as shown in Fig. 4(d). Our analysis based on the g-tensor explains previous studies on kagome materials [50,51,53,54,75,77] with a fresh mechanism in terms of altermagnetism.

In conclusion, we have demonstrated that WFM can be induced in AMs by the alternating g-tensor anisotropy Δg, which is a distinguishing feature of AMs that sets them apart from conventional AFMs. This mechanism applies to AMs with either collinear or noncollinear spin structures. The concept of Δg is useful for classifying type-I and type-II AMs. Our theory provides new understanding of the WFM in general and proposes ways to manipulate magnetic configurations in various AMs. We suggest further investigations on its role in novel AMs with twisted [78,79], Janus [79–81], or supercell [82] structures. Finally, our findings suggest that AMs could act as orbital ferromagnets, where emergent orbital effects are potentially linked to Δg. This opens a promising research direction toward orbital engineering, e.g., orbitronics [83,84] utilizing AMs.

Acknowledgments—D. J. and P. M. O. were supported by the Swedish Research Council (VR), the Knut and Alice Wallenberg Foundation (Grants No. 2022.0079 and No. 2023.0336), and the Wallenberg Initiative Materials Science for Sustainability (WISE) funded by the Knut and Allice Wallenberg Foundation. D. G., Y. M., and P. M. O. acknowledge funding from the European Union's HORIZON EUROPE, under Grant Agreement No. 101129641, "OBELIX", and D. G. and Y. M. acknowledge financial support by the Deutsche Forschungsgemeinschaft (DFG, German Research Foundation)-TRR 288-422213477 (Project No. B06) and TRR 173/3-268565370 (Project No. A11). S.-W. C. was supported by the U.S. DOE under Grant No. DOE: DE-FG02-07ER46382. H.-W. L. was supported by the National Research Foundation of Korea (NRF) (No. RS-2024-00356270 and No. RS-2024-00410027). The calculations were supported by resources provided by the National Academic Infrastructure for Supercomputing in Sweden (NAISS) at NSC Linköping, partially funded by VR through Grant No. 2022-06725.

Data availability—No data were created or analyzed in this study.

[1] Y. Noda, K. Ohno, and S. Nakamura, Momentum-dependent band spin splitting in semiconducting $\mathrm{MnO_2}$: A density functional calculation, Phys. Chem. Chem. Phys. **18**, 13294 (2016).

[2] K.-H. Ahn, A. Hariki, K.-W. Lee, and J. Kuneš, Antiferromagnetism in $\mathrm{RuO_2}$ as d-wave Pomeranchuk instability, Phys. Rev. B **99**, 184432 (2019).

[3] M. Naka, S. Hayami, H. Kusunose, Y. Yanagi, Y. Motome, and H. Seo, Spin current generation in organic antiferromagnets, Nat. Commun. **10**, 4305 (2019).

[4] S. Hayami, Y. Yanagi, and H. Kusunose, Momentum-dependent spin splitting by collinear antiferromagnetic ordering, J. Phys. Soc. Jpn. **88**, 123702 (2019).

[5] L. Šmejkal, R. González-Hernández, T. Jungwirth, and J. Sinova, Crystal time-reversal symmetry breaking and spontaneous Hall effect in collinear antiferromagnets, Sci. Adv. **6**, eaaz8809 (2020).

[6] L.-D. Yuan, Z. Wang, J.-W. Luo, E. I. Rashba, and A. Zunger, Giant momentum-dependent spin splitting in centrosymmetric low-Z antiferromagnets, Phys. Rev. B **102**, 014422 (2020).

[7] S. Hayami, Y. Yanagi, and H. Kusunose, Bottom-up design of spin-split and reshaped electronic band structures in antiferromagnets without spin-orbit coupling: Procedure on the basis of augmented multipoles, Phys. Rev. B **102**, 144441 (2020).

[8] H. Reichlová *et al.*, Macroscopic time reversal symmetry breaking by staggered spin-momentum interaction, arXiv:2012.15651.

[9] L.-D. Yuan, Z. Wang, J.-W. Luo, and A. Zunger, Prediction of low-Z collinear and noncollinear antiferromagnetic

compounds having momentum-dependent spin splitting even without spin-orbit coupling, Phys. Rev. Mater. **5**, 014409 (2021).

[10] M. Naka, Y. Motome, and H. Seo, Perovskite as a spin current generator, Phys. Rev. B **103**, 125114 (2021).

[11] R. González-Hernández, L. Šmejkal, K. Výborný, Y. Yahagi, J. Sinova, T. Jungwirth, and J. Železný, Efficient electrical spin splitter based on nonrelativistic collinear antiferromagnetism, Phys. Rev. Lett. **126**, 127701 (2021).

[12] H.-Y. Ma, M. Hu, N. Li, J. Liu, W. Yao, J.-F. Jia, and J. Liu, Multifunctional antiferromagnetic materials with giant piezomagnetism and noncollinear spin current, Nat. Commun. **12**, 2846 (2021).

[13] L.-D. Yuan, Z. Wang, J.-W. Luo, and A. Zunger, Strong influence of nonmagnetic ligands on the momentum-dependent spin splitting in antiferromagnets, Phys. Rev. B **103**, 224410 (2021).

[14] X. Zhou, W. Feng, X. Yang, G.-Y. Guo, and Y. Yao, Crystal chirality magneto-optical effects in collinear antiferromagnets, Phys. Rev. B **104**, 024401 (2021).

[15] S. A. Egorov, D. B. Litvin, and R. A. Evarestov, Antiferromagnetism-induced spin splitting in systems described by magnetic layer groups, J. Phys. Chem. C **125**, 16147 (2021).

[16] I. I. Mazin, K. Koepernik, M. D. Johannes, R. González-Hernández, and L. Šmejkal, Prediction of unconventional magnetism in doped $FeSb_2$, Proc. Natl. Acad. Sci. U.S.A. **118**, e2108924118 (2021).

[17] D.-F. Shao, S.-H. Zhang, M. Li, C.-B. Eom, and E. Y. Tsymbal, Spin-neutral currents for spintronics, Nat. Commun. **12**, 7061 (2021).

[18] L. Šmejkal, A. B. Hellenes, R. González-Hernández, J. Sinova, and T. Jungwirth, Giant and tunneling magnetoresistance in unconventional collinear antiferromagnets with nonrelativistic spin-momentum coupling, Phys. Rev. X **12**, 011028 (2022).

[19] L. Šmejkal, J. Sinova, and T. Jungwirth, Beyond conventional ferromagnetism and antiferromagnetism: A phase with nonrelativistic spin and crystal rotation symmetry, Phys. Rev. X **12**, 031042 (2022).

[20] L. Šmejkal, J. Sinova, and T. Jungwirth, Emerging research landscape of altermagnetism, Phys. Rev. X **12**, 040501 (2022).

[21] I. Mazin (The PRX Editors), Editorial: Altermagnetism—A new punch line of fundamental magnetism, Phys. Rev. X **12**, 040002 (2022).

[22] H. Chen, L. Liu, X. Zhou, Z. Meng, X. Wang, Z. Duan, G. Zhao, H. Yan, P. Qin, and Z. Liu, Emerging antiferromagnets for spintronics, Adv. Mater. **36**, 2310379 (2024).

[23] L. Bai, W. Feng, S. Liu, L. Šmejkal, Y. Mokrousov, and Y. Yao, Altermagnetism: Exploring new frontiers in magnetism and spintronics, Adv. Funct. Mater. **34**, 2409327 (2024).

[24] O. Fedchenko *et al.*, Observation of time-reversal symmetry breaking in the band structure of altermagnetic RuO_2, Sci. Adv. **10**, eadj4883 (2024).

[25] J. Krempaský *et al.*, Altermagnetic lifting of Kramers spin degeneracy, Nature (London) **626**, 517 (2024).

[26] Y.-P. Zhu *et al.*, Observation of plaid-like spin splitting in a noncoplanar antiferromagnet, Nature (London) **626**, 523 (2024).

[27] A. Hariki, A. Dal Din, O. J. Amin, T. Yamaguchi, A. Badura, D. Kriegner, K. W. Edmonds, R. P. Campion, P. Wadley, D. Backes, L. S. I. Veiga, S. S. Dhesi, G. Springholz, L. Šmejkal, K. Výborný, T. Jungwirth, and J. Kuneš, X-ray magnetic circular dichroism in altermagnetic α-MnTe, Phys. Rev. Lett. **132**, 176701 (2024).

[28] L. Šmejkal, A. H. MacDonald, J. Sinova, S. Nakatsuji, and T. Jungwirth, Anomalous Hall antiferromagnets, Nat. Rev. Mater. **7**, 482 (2022).

[29] Z. Feng, X. Zhou, L. Šmejkal, L. Wu, Z. Zhu, H. Guo, R. González-Hernández, X. Wang, H. Yan, P. Qin, X. Zhang, H. Wu, H. Chen, Z. Meng, L. Liu, Z. Xia, J. Sinova, T. Jungwirth, and Z. Liu, An anomalous Hall effect in altermagnetic ruthenium dioxide, Nat. Electron. **5**, 735 (2022).

[30] A. Bose, N. J. Schreiber, R. Jain, D.-F. Shao, H. P. Nair, J. Sun, X. S. Zhang, D. A. Muller, E. Y. Tsymbal, D. G. Schlom, and D. C. Ralph, Tilted spin current generated by the collinear antiferromagnet ruthenium dioxide, Nat. Electron. **5**, 267 (2022).

[31] H. Bai, L. Han, X. Y. Feng, Y. J. Zhou, R. X. Su, Q. Wang, L. Y. Liao, W. X. Zhu, X. Z. Chen, F. Pan, X. L. Fan, and C. Song, Observation of spin splitting torque in a collinear antiferromagnet RuO_2, Phys. Rev. Lett. **128**, 197202 (2022).

[32] S. Karube, T. Tanaka, D. Sugawara, N. Kadoguchi, M. Kohda, and J. Nitta, Observation of spin-splitter torque in collinear antiferromagnetic RuO_2, Phys. Rev. Lett. **129**, 137201 (2022).

[33] I. Žutić, J. Fabian, and S. Das Sarma, Spintronics: Fundamentals and applications, Rev. Mod. Phys. **76**, 323 (2004).

[34] A. Hirohata, K. Yamada, Y. Nakatani, I.-L. Prejbeanu, B. Diény, P. Pirro, and B. Hillebrands, Review on spintronics: Principles and device applications, J. Magn. Magn. Mater. **509**, 166711 (2020).

[35] T. Jungwirth, X. Marti, P. Wadley, and J. Wunderlich, Antiferromagnetic spintronics, Nat. Nanotechnol. **11**, 231 (2016).

[36] V. Baltz, A. Manchon, M. Tsoi, T. Moriyama, T. Ono, and Y. Tserkovnyak, Antiferromagnetic spintronics, Rev. Mod. Phys. **90**, 015005 (2018).

[37] S. Bhowal and N. A. Spaldin, Ferroically ordered magnetic octupoles in d-wave altermagnets, Phys. Rev. X **14**, 011019 (2024).

[38] P. A. McClarty and J. G. Rau, Landau theory of altermagnetism, Phys. Rev. Lett. **132**, 176702 (2024).

[39] C. Autieri, R. M. Sattigeri, G. Cuono, and A. Fakhredine, Dzyaloshinskii-Moriya interaction inducing weak ferromagnetism in centrosymmetric altermagnets and weak ferrimagnetism in noncentrosymmetric altermagnets, Phys. Rev. B **111**, 054442 (2025).

[40] R. M. Fernandes, V. S. de Carvalho, T. Birol, and R. G. Pereira, Topological transition from nodal to nodeless Zeeman splitting in altermagnets, Phys. Rev. B **109**, 024404 (2024).

[41] D. S. Antonenko, R. M. Fernandes, and J. W. F. Venderbos, Mirror Chern bands and Weyl nodal loops in altermagnets, Phys. Rev. Lett. **134**, 096703 (2025).

[42] M. Milivojević, M. Orozović, S. Picozzi, M. Gmitra, and S. Stavrić, Interplay of altermagnetism and weak ferromagnetism in two-dimensional RuF_4, 2D Mater. **11**, 035025 (2024).

[43] S.-W. Cheong and F.-T. Huang, Altermagnetism with noncollinear spins, npj Quantum Mater. **9**, 13 (2024).

[44] K. P. Kluczyk, K. Gas, M. J. Grzybowski, P. Skupiński, M. A. Borysiewicz, T. Fąs, J. Suffczyński, J. Z. Domagala, K. Grasza, A. Mycielski, M. Baj, K. H. Ahn, K. Výborný, M. Sawicki, and M. Gryglas-Borysiewicz, Coexistence of anomalous Hall effect and weak magnetization in a nominally collinear antiferromagnet MnTe, Phys. Rev. B **110**, 155201 (2024).

[45] S.-W. Cheong and F.-T. Huang, Altermagnetism classification, npj Quantum Mater. **10**, 38 (2025).

[46] I. Dzyaloshinsky, A thermodynamic theory of "weak" ferromagnetism of antiferromagnetics, J. Phys. Chem. Solids **4**, 241 (1958).

[47] T. Moriya, Anisotropic superexchange interaction and weak ferromagnetism, Phys. Rev. **120**, 91 (1960).

[48] S.-W. Cheong, J. D. Thompson, and Z. Fisk, Metamagnetism in La_2CuO_4, Phys. Rev. B **39**, 4395 (1989).

[49] L. M. Sandratskii and J. Kübler, Role of orbital polarization in weak ferromagnetism, Phys. Rev. Lett. **76**, 4963 (1996).

[50] J. Kübler and C. Felser, Non-collinear antiferromagnets and the anomalous Hall effect, Europhys. Lett. **108**, 67001 (2014).

[51] H. Chen, T.-C. Wang, D. Xiao, G.-Y. Guo, Q. Niu, and A. H. MacDonald, Manipulating anomalous Hall antiferromagnets with magnetic fields, Phys. Rev. B **101**, 104418 (2020).

[52] T. Moriya, Theory of magnetism of NiF_2, Phys. Rev. **117**, 635 (1960).

[53] S. Tomiyoshi and Y. Yamaguchi, Magnetic structure and weak ferromagnetism of Mn_3Sn studied by polarized neutron diffraction, J. Phys. Soc. Jpn. **51**, 2478 (1982).

[54] T. Nagamiya, S. Tomiyoshi, and Y. Yamaguchi, Triangular spin configuration and weak ferromagnetism of Mn_3Sn and Mn_3Ge, Solid State Commun. **42**, 385 (1982).

[55] C. Ederer and N. A. Spaldin, Weak ferromagnetism and magnetoelectric coupling in bismuth ferrite, Phys. Rev. B **71**, 060401(R) (2005).

[56] C. Kittel, On the gyromagnetic ratio and spectroscopic splitting factor of ferromagnetic substances, Phys. Rev. **76**, 743 (1949).

[57] P. Bruno, Tight-binding approach to the orbital magnetic moment and magnetocrystalline anisotropy of transition-metal monolayers, Phys. Rev. B **39**, 865 (1989).

[58] L. Alahmed, X. Zhang, J. Wen, Y. Xiong, Y. Li, L.-c. Zhang, F. Lux, F. Freimuth, M. Mahdi, Y. Mokrousov, V. Novosad, W.-K. Kwok, D. Yu, W. Zhang, Y. S. Lee, and P. Li, Evidence of magnon-mediated orbital magnetism in a quasi-2D topological magnon insulator, Nano Lett. **22**, 5114 (2022).

[59] N. Ito and K. Nomura, Anomalous Hall effect and spontaneous orbital magnetization in antiferromagnetic Weyl metal, J. Phys. Soc. Jpn. **86**, 063703 (2017).

[60] T. Moriya, Piezomagnetism in CoF_2, J. Phys. Chem. Solids **11**, 73 (1959).

[61] A. S. Disa, M. Fechner, T. F. Nova, B. Liu, M. Först, D. Prabhakaran, P. G. Radaelli, and A. Cavalleri, Polarizing an antiferromagnet by optical engineering of the crystal field, Nat. Phys. **16**, 937 (2020).

[62] See Supplemental Material at http://link.aps.org/supplemental/10.1103/PhysRevLett.134.196703 for details of the tight-binding models and the first-principle calculation, which includes Refs. [63–71].

[63] J. C. Slater and G. F. Koster, Simplified LCAO method for the periodic potential problem, Phys. Rev. **94**, 1498 (1954).

[64] The FLEUR project, https://www.flapw.de/.

[65] D. Wortmann *et al.*, FLEUR, Zenodo (2023).

[66] E. Wimmer, H. Krakauer, M. Weinert, and A. J. Freeman, Full-potential self-consistent linearized-augmented-plane-wave method for calculating the electronic structure of molecules and surfaces: O_2 molecule, Phys. Rev. B **24**, 864 (1981).

[67] J. P. Perdew, K. Burke, and M. Ernzerhof, Generalized gradient approximation made simple, Phys. Rev. Lett. **77**, 3865 (1996).

[68] C. Li, A. J. Freeman, H. J. F. Jansen, and C. L. Fu, Magnetic anisotropy in low-dimensional ferromagnetic systems: Fe monolayers on Ag(001), Au(001), and Pd(001) substrates, Phys. Rev. B **42**, 5433 (1990).

[69] I. P. R. Moreira, R. Dovesi, C. Roetti, V. R. Saunders, and R. Orlando, *Ab initio* study of MF_2 $(M = \mathrm{Mn, Fe, Co, Ni})$ rutile-type compounds using the periodic unrestricted Hartree-Fock approach, Phys. Rev. B **62**, 7816 (2000).

[70] H. J. Monkhorst and J. D. Pack, Special points for Brillouin-zone integrations, Phys. Rev. B **13**, 5188 (1976).

[71] G. Pizzi *et al.*, Wannier90 as a community code: New features and applications, J. Phys. Condens. Matter **32**, 165902 (2020).

[72] H. Thoma, V. Hutanu, H. Deng, V. E. Dmitrienko, P. J. Brown, A. Gukasov, G. Roth, and M. Angst, Revealing the absolute direction of the Dzyaloshinskii-Moriya interaction in prototypical weak ferromagnets by polarized neutrons, Phys. Rev. X **11**, 011060 (2021).

[73] M. Ikhlas, S. Dasgupta, F. Theuss, T. Higo, S. Kittaka, B. J. Ramshaw, O. Tchernyshyov, C. W. Hicks, and S. Nakatsuji, Piezomagnetic switching of the anomalous Hall effect in an antiferromagnet at room temperature, Nat. Phys. **18**, 1086 (2022).

[74] W. A. Harrison, *Electronic Structure and the Properties of Solids* (Dover, New York, 1989).

[75] H. Chen, Q. Niu, and A. H. MacDonald, Anomalous Hall effect arising from noncollinear antiferromagnetism, Phys. Rev. Lett. **112**, 017205 (2014).

[76] Y. Zhang, Y. Sun, H. Yang, J. Železný, S. P. P. Parkin, C. Felser, and B. Yan, Strong anisotropic anomalous Hall effect and spin Hall effect in the chiral antiferromagnetic compounds Mn_3X ($X =$ Ge, Sn, Ga, Ir, Rh, and Pt), Phys. Rev. B **95**, 075128 (2017).

[77] S. Nakatsuji, N. Kiyohara, and T. Higo, Large anomalous Hall effect in a non-collinear antiferromagnet at room temperature, Nature (London) **527**, 212 (2015).

[78] R. He, D. Wang, N. Luo, J. Zeng, K.-Q. Chen, and L.-M. Tang, Nonrelativistic spin-momentum coupling in antiferromagnetic twisted bilayers, Phys. Rev. Lett. **130**, 046401 (2023).

[79] S. Sheoran and S. Bhattacharya, Nonrelativistic spin splittings and altermagnetism in twisted bilayers of centrosymmetric antiferromagnets, Phys. Rev. Mater. **8**, L051401 (2024).

[80] I. Mazin, R. González-Hernández, and L. Šmejkal, Induced monolayer altermagnetism in MnP(S, Se)$_3$ and FeSe, arXiv:2309.02355.

[81] Y. Zhu, T. Chen, Y. Li, L. Qiao, X. Ma, C. Liu, T. Hu, H. Gao, and W. Ren, Multipiezo effect in altermagnetic V$_2$SeTeO monolayer, Nano Lett. **24**, 472 (2024).

[82] R. Jaeschke-Ubiergo, V. K. Bharadwaj, T. Jungwirth, L. Šmejkal, and J. Sinova, Supercell altermagnets, Phys. Rev. B **109**, 094425 (2024).

[83] D. Go, D. Jo, H.-W. Lee, M. Kläui, and Y. Mokrousov, Orbitronics: Orbital currents in solids, Europhys. Lett. **135**, 37001 (2021).

[84] D. Jo, D. Go, G.-M. Choi, and H.-W. Lee, Spintronics meets orbitronics: Emergence of orbital angular momentum in solids, npj Spintron. **2**, 19 (2024).

[85] I. E. Dzialoshinskii, The magnetic structure of fluorides of the transition metals, Sov. Phys. JETP **6**, 1120 (1958).

End Matter

Discussions on DMI—Here, we demonstrate that the DMI does not contribute to the WFM in the models examined in this study [e.g., Figs. 1(c)–1(e)]. The DMI, $E_{\mathrm{DMI}} = \mathbf{D}_{ij} \cdot (\mathbf{S}_i \times \mathbf{S}_j)$, between spins at sites i and j, is characterized by the DMI vector $\mathbf{D}_{ij}$, whose orientation is dictated by the crystal symmetry. For our model in Fig. 1(c), the crystal structure has two mirror planes—one horizontal and one vertical—including sublattices A and B. Since the DMI vector should be perpendicular to each mirror plane according to the Moriya's rules [47], the presence of the two symmetry planes implies that the DMI vector should be zero. On the other hand, for the kagome lattice shown in Figs. 1(d) and 1(e), there is only one mirror plane—horizontal—including all sublattices A, B, and C. Accordingly, the DMI vectors $\mathbf{D}_{ij}$ are identically oriented along the out-of-plane direction for all i and j, i.e., $\mathbf{D}_{AB} = \mathbf{D}_{BC} = \mathbf{D}_{CA} = D\hat{\mathbf{z}}$. The DMI energy is then given by $E_{\mathrm{DMI}} = D\hat{\mathbf{z}} \cdot (\mathbf{S}_A \times \mathbf{S}_B + \mathbf{S}_B \times \mathbf{S}_C + \mathbf{S}_C \times \mathbf{S}_A)$. Depending on the sign of D, the DMI energetically stabilizes either the normal ($D < 0$) [Fig. 1(d)] or inverse ($D > 0$) [Fig. 1(e)] triangular spin structure [53]. We emphasize that, in both spin structures, spins are fully compensated. Small deviations from these fully compensated spin structures can generate a finite net spin moment but increase E_{DMI}, indicating that the DMI does not produce a net magnetic moment. This consequence also shows that the g-tensor anisotropy mechanism can be the dominant contribution to the WFM, even in the presence of the DMI.

Although the DMI does not contribute to the WFM in our models, the g-tensor anisotropy and DMI mechanisms for WFM can coexist in other systems. To illustrate this, let us consider a fully compensated spin system. If we include SOC to this system, it can affect the compensation in two ways: (i) giving additional interaction terms to the spin Hamiltonian and (ii) inducing a local orbital moment. Effect (i) can lead to the spin rearrangement, e.g., spin canting due to the DMI, so that the canted spin configuration with finite net spin moment minimizes the energy. On the other hand, effect (ii) occurs independently of the spin rearrangement. Once the spin configuration is given, regardless of whether effect (i) is present or not, the local orbital moment is induced by the spin moment through SOC, with its magnitude and direction being associated with the local g-tensor. The correction to the net orbital moment due to (i) is proportional to the square of the SOC magnitude. Thus, as long as the SOC is weak, the magnitude and direction of the net orbital moment are essentially unaffected by (i) and the two processes (i) and (ii) make independent contributions to the net moment.

WFM in rutile-type AMs—In addition to the tight-binding models, we discuss the origin of WFM in rutile-type antiferromagnets [Fig. 5(a)], such as RuO$_2$ and NiF$_2$, which are regarded as prototypical AMs. These systems can exhibit the WFM for specific directions of the Néel vector. For example, a recent first-principles calculation [5] reported that, in RuO$_2$, a net magnetic moment is induced along the b axis when the Néel vector is along the a axis. Although this WFM was attributed to the DMI in the recent study, it cannot be explained by the conventional DMI mechanism, which involves an antisymmetric exchange interaction $\mathbf{D}_{AB} \cdot (\mathbf{S}_A \times \mathbf{S}_B)$ between spins at sublattices A and B. For the DMI to induce spin canting in the a-b plane, the DMI vector $\mathbf{D}_{AB}$ must point along the c axis. However, by Moriya's rules [47], the c component of $\mathbf{D}_{AB}$ is forbidden due to the presence of a vertical mirror plane containing sublattices A and B [Fig. 5(b)]. Indeed, an earlier study by Dzyaloshinskii [85] demonstrated that the rutile structure does not exhibit the antisymmetric exchange interaction. Additionally, Moriya [52] explained the WFM in NiF$_2$ as arising from single-ion anisotropy. This explanation aligns with our g-tensor

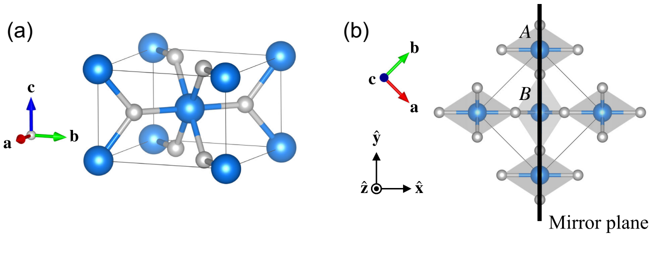

FIG. 5. (a) Crystal structure of a rutile-type AM, where blue and gray spheres represent magnetic and nonmagnetic ions, respectively. (b) Top view of the structure. The black solid line indicates the mirror plane (110) that includes two magnetic sublattices, A and B.

TABLE I. The a, b, and c components of spin ($\mathbf{m}^{\mathrm{spin}}$) and orbital ($\mathbf{m}^{\mathrm{orb}}$) magnetic moments for Ni atoms at sublattices A and B.

Atom	m_a^{spin} (μ_{B})	m_b^{spin} (μ_{B})	m_c^{spin} (μ_{B})	m_a^{orb} (μ_{B})	m_b^{orb} (μ_{B})	m_c^{orb} (μ_{B})
Ni A	-1.72	-2.3×10^{-4}	0	-0.16	-2.5×10^{-3}	0
Ni B	1.72	-2.3×10^{-4}	0	0.16	-2.5×10^{-3}	0

anisotropy mechanism from a symmetry perspective, though it did not recognize the importance of the orbital moment. Our work goes beyond the Moriya's explanation by considering the orbital moment and shows that the net orbital moment dominates over the net spin moment in rutile-type AMs such as RuO_2 [5] and NiF_2 (see below), highlighting the g-tensor anisotropy mechanism as the most relevant mechanism for the WFM in these materials.

First-principles calculation for NiF_2—We show that the g-tensor anisotropy mechanism plays a dominant role in the WFM of a rutile AM using the density functional theory code FLEUR [64,65] based on the full-potential linearized augmented plane-wave method [66] (see Supplemental Material [62] for details). Specifically, we calculated spin and orbital magnetic moments in insulating NiF_2 [Fig. 5], where initial spin moments for Ni A and Ni B sublattices are aligned along $-\mathbf{a}$ and $+\mathbf{a}$, respectively, and then relaxed after including the atomic SOC. Table I presents the calculated spin and orbital magnetic moments for each Ni atom. The resulting magnetic moment deviates from the initial direction ($-\mathbf{a}$ or $+\mathbf{a}$), leading to a net magnetic moment along the b axis, where the orbital contribution (m_b^{orb}) dominates over the spin contribution (m_b^{spin}). This dominance of the orbital contribution and the net magnetic moment direction [Eq. (4) with $\phi = -45°$] are consistent with our mechanism based on the g-tensor anisotropy. We note that this result cannot be attributed to the DMI, as discussed in the previous paragraph.

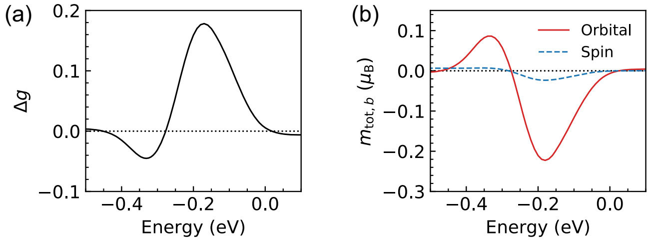

FIG. 6. (a) Local g-tensor anisotropy (Δg) of the Ni atom in NiF_2 as a function of the Fermi energy. (b) Orbital and spin contributions to the net magnetic moment in NiF_2.

The net moment in NiF_2 is relatively small since Δg is weak in an insulating phase, but the Δg and the resulting net moment can be significantly enhanced by doping. To investigate this, we evaluated Δg in NiF_2 as a function of the Fermi energy. The local g-tensor elements at the Ni atom can be obtained by $g_{\parallel} = 2 + \langle L_x^A \rangle / \langle S_x^A \rangle$ and $g_{\perp} = 2 + \langle L_y^A \rangle / \langle S_y^A \rangle$ [see Fig. 5(b) for the axis convention]. The local g-tensor anisotropy is then given by $\Delta g = g_{\parallel} - g_{\perp}$. Figure 6(a) shows that the calculated Δg significantly increases with p-doping, reaching the order of 0.1. Consequently, the net magnetic moment becomes larger, with the orbital contribution dominating over the spin contribution [Fig. 6(b)]. Notably, the magnitude and energy dependence of Δg and the net moment align well with our tight-binding results [Figs. 3(c) and 3(d)]. This large net orbital moment on the order of $0.1\mu_{\mathrm{B}}$ in the metallic phase is also consistent with first-principles calculations for the altermagnetic metal RuO_2 [5].